



# Hydrogen production by bioethanol partial oxidation over Ni based catalysts



Elka Kraleva <sup>a,\*</sup>, Marga-Martina Pohl <sup>a</sup>, Astrid Jürgensen <sup>b</sup>, Heike Ehrich <sup>a</sup>

<sup>a</sup> Leibniz Institute for Catalysis (LIKAT), Albert-Einstein-Str. 29a, D-18059 Rostock, Germany

<sup>b</sup> Leibniz Institut für Analytische Wissenschaften – ISAS – e.V., Bunsen-Kirchhoff-Straße 11, D-44137 Dortmund, Germany

## ARTICLE INFO

### Article history:

Received 27 January 2015

Received in revised form 29 May 2015

Accepted 2 June 2015

Available online 6 June 2015

### Keywords:

Bioethanol

Partial oxidation

Hydrogen production

xNiAlZn catalysts

## ABSTRACT

The xNiAlZn catalysts with different Ni loading ( $x = 5, 10$  and  $20$  wt%) and nearly constant Al/Zn weight ratio ( $\text{Al/Zn} = 0.73$ ) were prepared by the citrate method and characterized by different techniques –  $S_{\text{BET}}$ , TPR, XRD, XPS, and TEM. The influence of parameters, such as reaction temperature, oxygen-to-fuel molar ratio, and Ni loading on hydrogen production was investigated. The catalysts were active in the partial oxidation of ethanol at atmospheric pressure in the temperature range  $600$ – $750$  °C. The conversion was always complete at temperatures above  $600$  °C, regardless of the changes in other reaction conditions. A syngas is produced which can be used in solid oxide fuel cell applications. Selectivity to hydrogen and CO increased with increasing temperature and decreased with increasing Ni loading. The highest selectivity ( $S$ ) was obtained over 5NiAlZn. At  $700$  °C this sample showed  $S(\text{H}_2)$  of 90%,  $S(\text{CO})$  of 92%, and only small amounts of byproducts such as  $\text{CO}_2$  and  $\text{CH}_4$  were detected. Morphological and structural modifications in the catalysts under reaction conditions, determined by the amount of nickel, were closely related to the activity of the samples. The effect of the parameters on side reactions and distribution of byproducts were also discussed. During  $100$  h time-on-stream, ethanol conversion and selectivity to  $\text{H}_2$  and CO over 5NiAlZn and 10NiAlZn remained unchanged demonstrating stable performance of the catalysts. Additionally, the stability of the Ni catalyst was studied by means of simulated start-stop operation cycles during the partial oxidation reaction to simulate thermal cycles during the solid oxide fuel cell lifetime. With increasing number of thermal cycles a slight decline in ethanol conversion was observed and the selectivity to hydrogen and CO decreased. By using a molar ratio oxygen/ethanol of 0.75 a syngas with high selectivity to  $\text{H}_2$  and CO was obtained.

© 2015 Elsevier B.V. All rights reserved.

## 1. Introduction

The key role of hydrogen in the world energy system depends greatly on the production from renewable sources and the implementation of fuel cells in the economy. Fuel cells have attracted a lot of attention as one of the alternative sources of clean energy [1,2]. Among different possible alternatives to produce energy, the system based on fuel cells (FCs) presents two characteristics that make it an attractive option: (i) the enhancement of the overall process efficiency by direct transformation of chemical energy to electricity, and (ii) the extension of present energy sources, as FCs work with hydrogen, which can be produced from a large variety of feed stocks, including fossil fuels and renewable resources [3]. Various fuel cells have been used in stationary power plants, mobile

devices, and space missions so far. However, the proton exchange membrane fuel cell (PEM) working at low temperatures and the high temperature solid oxide fuel cell (SOFC) have been identified as the most promising technologies for future markets [1]. The main advantage of the SOFC technology is its high flexibility regarding the fuel. Due to the high operating temperature, the SOFC is able to convert many fuels such as natural gas, propane, methanol, ethanol or biogas into electrical energy. Additionally, this system shows a high tolerance to impurities in the inlet fuel. Solid oxide fuel cells are of particular interest because of their high efficiency of up to 80%, which can be obtained by the co-generation of power and heat [4].

Bioethanol is considered to be an attractive alternative fuel based on renewable energy sources. Compared to other green fuels, the high safety in storage and handling, together with the high energy density, are the main advantages. In preliminary tests bioethanol of technical quality (97 vol%) has been used successfully as a fuel for hydrogen generation in model SOFC [5]. Currently, there

\* Corresponding author. Fax: +49 381 1281 51330.

E-mail address: [elka.kraleva@catalysis.de](mailto:elka.kraleva@catalysis.de) (E. Kraleva).

are three catalytic routes for converting ethanol to syngas, which is produced by internal reforming in the FCs: steam reforming (SR), partial oxidation (POX) and auto thermal reforming (ATR). Steam reforming provides high efficiency and reformate quality, i.e., a high hydrogen yield and a low rate of side reactions, but it suffers from some disadvantages, such as high energy consumption. Compared to the SR process, POX and ATR feature fast start-up and response times because of the exothermic nature of the oxidation reaction [6]. In addition, the partial oxidation reaction requires lower energy for fuel evaporation because water is not needed. Air is used as an oxidant, thus eliminating the need for pure oxygen. All these features make the partial oxidation reaction attractive for mobile applications, where a compact system is required. The simplicity of the system design guarantees high efficiency and low system costs.

Based on thermodynamic calculations, the optimal operation conditions for partial oxidation of ethanol (POE) for hydrogen production are a temperature range between 800 and 1000 °C, an oxygen-to-ethanol molar ratio of 0.6–0.8, and atmospheric pressure. Under these conditions, complete conversion of ethanol and a hydrogen yield of 86–95% can be achieved without coke formation [7]. The hydrogen-rich fuel obtained makes POE suitable for SOFC applications, and so does the high content of CO in the reformate obtained, which acts as a fuel in SOFCs. The POE involves a complex reaction system with many undesirable side reactions. The relative importance of each of these reaction pathways depends on the selected reaction conditions and the choice of catalyst. However, each catalyst induces different pathways and, therefore, the selection of a suitable catalyst plays a vital role in the partial oxidation of ethanol for hydrogen production. Active catalysts should maximize hydrogen and CO selectivity, inhibit coke formation, and reduce CO<sub>2</sub> production.

So far, a variety of catalytic systems with different active metals have been studied for POE. Supported noble metals (Pd, Pt, Rh, Ir) were shown to have significant activity [8,9], but high costs limit their application. Instead, it is more practical to develop a cheap and effective catalyst for more economical benefits. As a less expensive alternative, increased attention has been concentrated on the development of non-noble metal catalysts, such as Co- and Ni-based materials [10,11]. Thanks to their ability to break CC bonds and the low selectivity to methane, Ni-based catalysts proved to be promising low cost candidates for effective hydrogen production by POE [12].

In our previous studies we reported that nickel and cobalt catalysts supported on binary mixed oxides present high activity in the partial oxidation of ethanol and high selectivity to hydrogen and CO [13–16]. The most active catalyst was a Ni catalyst based on AlZnO<sub>x</sub> as support, a thermally stable mixed oxide with amphoteric character, prepared by a citrate sol–gel method. The resulting powders were characterized by various techniques to examine the effect of phase composition on reducibility, structural and morphological properties, and finally, catalytic activity and stability [15,16].

The aim of the present study is to investigate the influence of Ni loading on the formation of crystal morphology and on the distribution of the catalytic active species in the bulk and on the surface of the AlZn supported catalyst. Catalysts with varying Ni content (5–20 wt%) were prepared by the citrate sol–gel method and characterized by nitrogen sorption, temperature-programmed reduction, high resolution transmission electron microscopy, X-ray photoelectron spectroscopy, and X-ray powder diffraction measurements. Finally, the effect of catalyst composition and morphology on the activity and hydrogen production in the partial oxidation of ethanol is studied. With respect to a commercial application of the catalysts for direct fuel reforming in a fuel cell of SOFC type, the lifetime of the catalyst has been studied by long-term stability tests over 100 h as well as by simulated start–stop cycling.

## 2. Experimental

### 2.1. Catalyst preparation

The NiAlZn catalysts with different Ni loading (5, 10 and 20 wt%) over a AlZnO<sub>x</sub> mixed oxide support were prepared by the citrate method. The target molar ratio of Al/Zn was 0.73. Metal nitrates Ni(NO<sub>3</sub>)<sub>2</sub>•6H<sub>2</sub>O (Merck), Zn(NO<sub>3</sub>)<sub>2</sub>•6H<sub>2</sub>O (Sigma–Aldrich), and Al(NO<sub>3</sub>)<sub>3</sub>•9H<sub>2</sub>O (Sigma–Aldrich) were used as precursors. The appropriate amounts of the nitrates were dissolved in water. Referred to the amount of metal cations, an equimolar amount of citric acid (Alfa Aesar) was added to the aqueous nitrate solution and stirred for 10 min. The temperature was raised to 75 °C for 30 min to form a homogeneous chelate of the metal cations and the citrate anions. The solution was concentrated in vacuum with a rotary evaporator at 75 °C until a viscous liquid was obtained. Dehydration was completed by drying the sample in a vacuum oven at 120 °C for 16 h followed by calcination at 450 °C for 2 h, then 500 °C for 5 h and finally 700 °C for 2 h under air flow. The high calcination temperature was chosen to ensure structure stability of the catalyst within the temperature range used for ethanol partial oxidation [13]. The non-promoted binary mixed oxide named AlZn was prepared under identical conditions. The samples were denoted by xNiAlZn where “x” indicates the Ni weight%.

### 2.2. Catalyst characterization

The specific surface area and porosity of the supports were calculated from the nitrogen adsorption–desorption isotherms collected at 196 °C with a BELSORP-mini II (BEL Japan, Inc.) surface area and pore size analyzer. Prior to the measurements, the samples were outgassed for 2 h at 250 °C. The specific surface area was calculated using the Brunauer, Emmet and Teller (BET) equation for the N<sub>2</sub> relative pressure range of 0.05 < p/p<sub>0</sub> < 0.30. Pore size distribution was determined by the Barrett–Joyner–Halenda (BJH) method from a desorption branch of the isotherm.

The elemental composition of the supports and catalysts was determined by inductively coupled plasma optical emission spectroscopy (ICP-OES) on a Varian 715-ES spectrometer. The amount of carbon deposited on the samples after the catalytic experiments was measured with a TruSpec Micro CHNS analyzer (LECO) equipped with a thermal conductivity detector.

X-ray powder diffraction (XRD) measurements were carried out on a STADI P automated transmission diffractometer (STOE, Darmstadt) with Cu K $\alpha$  radiation and a Ge monochromator. The patterns were collected in the 2 $\theta$  range of 5–60° in 0.5° steps with the dwell time of 100 s and recorded with a STOE position sensitive detector. The apparent size of the crystallites in the samples (spinel phases, nickel oxide and zinc oxide) was calculated by the Scherrer formula, L = 0.9 $\lambda$ / $\beta_{2\theta}$ cos $\theta_{max}$ , where  $\lambda$  is the X-ray wavelength (1.54056 Å for the Cu K $\alpha$  radiation),  $\beta_{2\theta}$  is the width of the ZnAl<sub>2</sub>O<sub>4</sub>, NiO and ZnO diffraction peaks at half-height, and  $\theta_{max}$  is the Bragg angle at the position of the peak maximum.

A high-resolution transmission electron microscopy (HRTEM) study was performed with an aberration-corrected JEM-ARM200F (JEOL, Corrector: CEOS) 200 kV transmission electron microscope. The microscope is equipped with a JED-2300 energy-dispersive X-ray-spectrometer (EDXS) for chemical analysis. The aberration corrected STEM imaging high-angle annular dark field (HAADF) and annular bright field (ABF) were performed with a spot size of approximately 0.13 nm, a convergence angle of 30–36°, and collection semi-angles for HAADF and ABF of 90–170 mrad and 11–22 mrad, respectively. For the TEM analysis the sample was deposited without any pretreatment onto a holey carbon supported Cu-grid (mesh 300) and then transferred into the microscope.

The XPS measurements were performed with an Axis HS spectrometer from Kratos Analytical. The measurements were done under high vacuum conditions ( $P < 3 \times 10^{-6}$  Pa) with X-ray excitation from an unmonochromatised Al anode ( $\text{Al K}\alpha$ ,  $h\nu = 1486.6$  eV, source operated at 9 kV and 20 mA) and with the concentric hemispherical analyzer set in electrostatic mode and operating in fixed analyzer transmission (FAT) mode for electron detection. The analyzer pass energy was set to 20 eV. The spectra were collected in the standard configuration with a takeoff angle of  $0^\circ$ , a charge balance of  $-30.4$  V was applied to compensate for sample charging, and the aperture lens was set to analyze a 2.1 mm diameter spot on the sample surface. A survey scan from 1400 to 0 eV binding energy and six region scans were collected for each sample. The region scans were the Zn 2p (1065–1005 eV,  $\Delta = 0.1$  eV,  $t = 300$  ms/pt), Ni 2p (900–840 eV,  $\Delta = 0.1$  eV,  $t = 300$  ms/pt), O 1s (550–515 eV,  $\Delta = 0.1$  eV,  $t = 300$  ms/pt), Zn L<sub>2,3</sub>M<sub>45</sub>M<sub>45</sub> (520–460 eV,  $\Delta = 0.1$  eV,  $t = 300$  ms/pt), and C 1s (305–270 eV,  $\Delta = 0.1$  eV,  $t = 300$  ms/pt) regions and a region covering the Zn 3s, Al 2s, Ni 3s, Zn 3p, Al 2p, and Ni 3p peaks (160–55 eV,  $\Delta = 0.1$  eV,  $t = 300$  ms/pt). Data analysis was performed using CasaXPS, version 2.3.15 [17]. After a Shirley background correction, the peaks in all spectra were fitted with 30% Gaussian – 70% Lorentzian product form functions. The Al K $\alpha_3$  and K $\alpha_4$  satellite peaks were fitted with position ( $E_B$ ), FWHM, and area (A) fixed relative to the corresponding main peak (Al K $\alpha_3$ :  $E_B = 9.8$  eV, FWHM = 0 eV, A  $\times 0.064$ ; K $\alpha_4$ :  $E_B = 11.8$  eV, FWHM = 0 eV, A  $\times 0.032$ ). Sample charging was corrected by setting the position of the main C 1s peak to 284.8 eV and shifting the spectra accordingly.

Temperature-programmed reduction (TPR) experiments were performed on 40–50 mg of each material. The materials were loaded into fixed-bed continuous flow quartz reactors and heated to 900 °C at 10 K/min in a 5% H<sub>2</sub>/Ar gas mixture passed at a flow rate of 7 mL/min. Hydrogen consumption and formation of water were monitored with a quadrupole mass spectrometer (Pfeiffer OmniStar). The total amount of hydrogen consumed by a sample was determined by integrating the profile of the MS signal.

### 2.3. Catalytic tests

Ethanol partial oxidation was carried out in a fixed bed flow reactor in a temperature range of 400–750 °C at atmospheric pressure. The operating temperature was regulated by a thermocouple inside the oven which was placed closed to the reactor. Activity tests were performed using 0.15 g of catalyst with a particle size range of 0.4–0.5 mm which was chosen after preliminary mass transport experiments to minimize diffusional resistances. The catalyst was diluted by quartz chips at a volume ratio of 1:10 to avoid adverse thermal effects. Catalyst particles were placed in the middle of a quartz-glass fixed-bed reactor. A thermocouple was inserted into the center of the catalyst bed to detect the reaction temperature. In the standard test, a feed with molar ratio of oxygen-to-ethanol of 0.75 was used. Environmentally sustainable bio-ethanol of 97 vol% purity (Richter GmbH) was used in all catalytic experiments. Ethanol was fed at a constant rate of 10 g/h to the evaporator heated to 120 °C and then mixed with a stream of air (291 mL/min) and N<sub>2</sub> (100 mL/min). The gas hourly space velocity (GHSV), defined as the ratio of the total volumetric flow to the catalyst volume, was 35,000 h<sup>-1</sup>. The catalysts were tested stepwise at target temperatures of 600, 700, and 750 °C, maintaining the reaction for 2 h at each temperature to check for a possible deactivation. The temperatures inside the catalyst bed were often higher ( $\sim 100$  K) because of thermal hot spots caused by the exothermic reaction.

In addition, the 5NiAlZn catalyst was used for catalytic tests with different oxygen-to-fuel ratios at 750 °C. The molar ratio of oxygen-to-ethanol ranged from 0.6 to 0.9. The same catalyst was chosen for stability tests. Catalyst degradation was checked under standard

conditions at 750 °C for 100 h. Thermal cycle stability tests were performed with start-and-stop simulation. An initial cycle of catalyst operation was run stepwise from 600 to 750 °C for 6 h, followed by a stop mode keeping the catalyst at room temperature for about 16 h. Then, the start-and-stop cycle was repeated until an overall operation time of 100 h with 4 cycles was obtained.

The composition of the inlet and outlet gas mixtures was frequently analyzed on-line using Shimadzu gas chromatographs equipped with FID and TCD detectors. The carbon balance calculated for each experiment was close to 1. To evaluate the catalyst performance, the conversion of ethanol and the selectivity with regard to hydrogen and to the carbon-containing products were calculated by Eqs. (1)–(3):

#### Conversion of ethanol

$$X_{\text{Ethanol}}(\%) = \frac{F_{\text{Ethanol,in}} - F_{\text{Ethanol,out}}}{F_{\text{Ethanol,in}}} \times 100 \quad (1)$$

#### Selectivity to hydrogen

$$S_{\text{H}_2}(\%) = \frac{F_{\text{H}_2}}{3 \times (F_{\text{Ethanol,in}} - F_{\text{Ethanol,out}})} \times 100 \quad (2)$$

#### Selectivity to carbon-containing products

$$S_i(\%) = \frac{F_{i,\text{out}}}{n_i \times (F_{\text{Ethanol,in}} - F_{\text{Ethanol,out}})} \times 100 \quad (3)$$

where  $F_i$  is the molar flow of the species  $i$  at the inlet (<sub>in</sub>) or outlet (<sub>out</sub>) of the reactor, and  $n_i$  is the stoichiometric factor between the carbon-containing  $i$ -species and ethanol.

## 3. Results and discussion

### 3.1. Structure and morphology of the catalysts

The elemental composition of the calcined AlZn support and the catalysts loaded with different amounts of Ni, their total surface area and the mean size of the crystallites, calculated based on XRD results by the Scherrer formula, are represented in Table 1. The elemental composition of the catalysts agrees well with the nominal composition. The Al/Zn mass ratio for all samples is about 0.3, which corresponds well to the given molar ratio of 0.73. Nitrogen sorption experiments performed on the prepared materials showed that the specific surface area of the catalysts is dramatically higher than that of the initial support. As shown in our previous study, this remarkable effect is only observed for catalysts prepared by a one-step method, indicating the high degree of incorporation of the Ni promoter into the structure of the mixed oxide [15]. The textural properties of the catalysts are influenced by the amount of Ni too. The increasing Ni loading resulted in an increasing surface area after calcination.

The X-ray patterns of the catalysts calcined at 700 °C are shown in Fig. 1. Diffraction patterns of all materials show intense and symmetric peaks of a ZnAl<sub>2</sub>O<sub>4</sub> spinel phase ( $2\theta = 31.2^\circ, 36.8^\circ, 55.7^\circ, 59.3^\circ, 65.3^\circ$ , PDF-No. [5–669]) indicating a high crystallinity of the samples [18]. Besides this spinel phase, signals of zinc oxide appear in all catalysts ( $2\theta = 31.8^\circ, 34.4^\circ, 36.2^\circ$ , PDF-No. [36–1451]). In the patterns of the Ni catalysts, reflections of NiO ( $2\theta = 37.3^\circ, 43.3^\circ, 62.9^\circ$ , PDF-No. [4–835]) were detected. However, since NiAl<sub>2</sub>O<sub>4</sub> (PDF-No. [78–0552]) and ZnAl<sub>2</sub>O<sub>4</sub> spinel have a lattice with very similar parameters, their reflections overlap, which makes the two phases indistinguishable. Thus both phases might be present in the catalysts. Reflections of Al<sub>2</sub>O<sub>3</sub> are absent, however their presence could not be ruled out. Al<sub>2</sub>O<sub>3</sub> usually shows poor crystallinity and its amount should be small due to the consumption of alumina in the spinel formation. Generally, an increase of Ni loading influences the phase distribution of the catalytic material and shifts the ratio of

**Table 1**

Physicochemical characteristics of the catalysts.

Samples	Ni (wt%)	Al (wt%)	Zn (wt%)	Al/Zn (wt/wt)	S <sub>BET</sub> (m <sup>2</sup> /g)	Crystallite size (nm) <sup>a</sup>		
						ZnAl <sub>2</sub> O <sub>4</sub>	ZnO	NiO
AlZn	0	15.6	51.7	0.30	3	24.5	17.9	
5NiAlZn	4.8	13.9	45.2	0.31	21	15.2	12.4	<3
10NiAlZn	9.2	14.0	45.2	0.31	29	12.6	12.4	6.8
20NiAlZn	19.5	13.9	45.1	0.31	40	11.5	15.2	9.2

<sup>a</sup> Determined by XRD – calculated by the Scherrer formula.

ZnO to spinel structure. The lower quantity of ZnAl<sub>2</sub>O<sub>4</sub> is probably due to an increased NiAl<sub>2</sub>O<sub>4</sub> formation. Furthermore, the formation of NiO is observed to increase upon Ni loading.

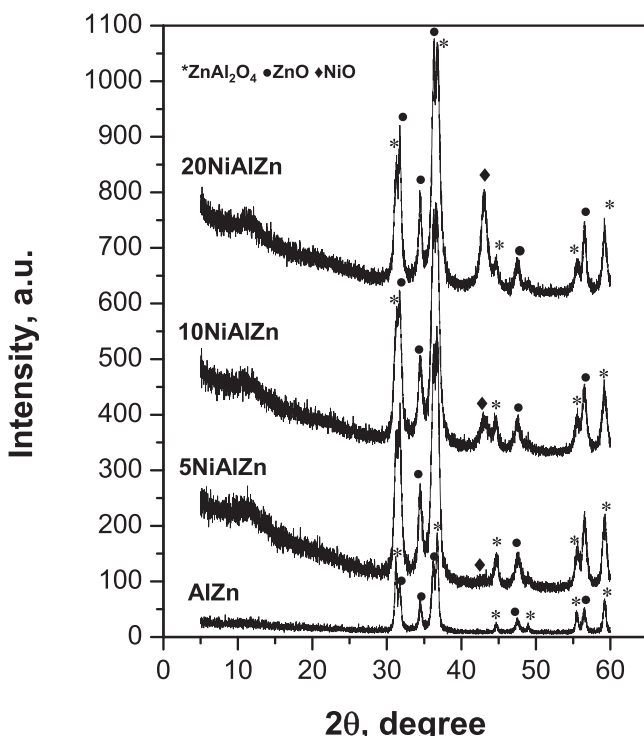
The crystallite sizes of the ZnAl<sub>2</sub>O<sub>4</sub>, ZnO and NiO phases estimated by the Scherrer equation are reported in Table 1. The results show clearly that the crystallite size of the phases depends on the nickel loading of the respective catalyst. The crystallite size of the NiO species consistently increased with increasing metal loading. However, it has to be stated here that the NiO peak in the 5NiAlZn sample is smaller than the size limit necessary for quantification by the Scherrer equation. The crystallite size of the ZnAl<sub>2</sub>O<sub>4</sub> spinel phase dropped drastically upon initial Ni incorporation, and decreased slightly as the metal loading was increased. The crystallite size of ZnO ranged from 17.9 nm to 12.4 nm with a rather unspecific influence of the Ni loading. Generally, a strong bonding of the support to the metal phases (NiO and NiAl<sub>2</sub>O<sub>4</sub>) stabilizes the phases, whereas weakly bonded metal phases may tend to collide and accumulate, forming larger crystallites. This might be a plausible reason for the relationship between crystallite size and metal content, although it is often difficult to explain the factors affecting the metal dispersion. The existence of larger particles on the surface of the catalyst is not favorable, as it causes nickel agglomeration and carbon formation on the catalyst, which affects the catalytic activity [19–21]. Interestingly, the NiO crystallite sizes of catalysts prepared with the citrate method were smaller than those synthesized by the

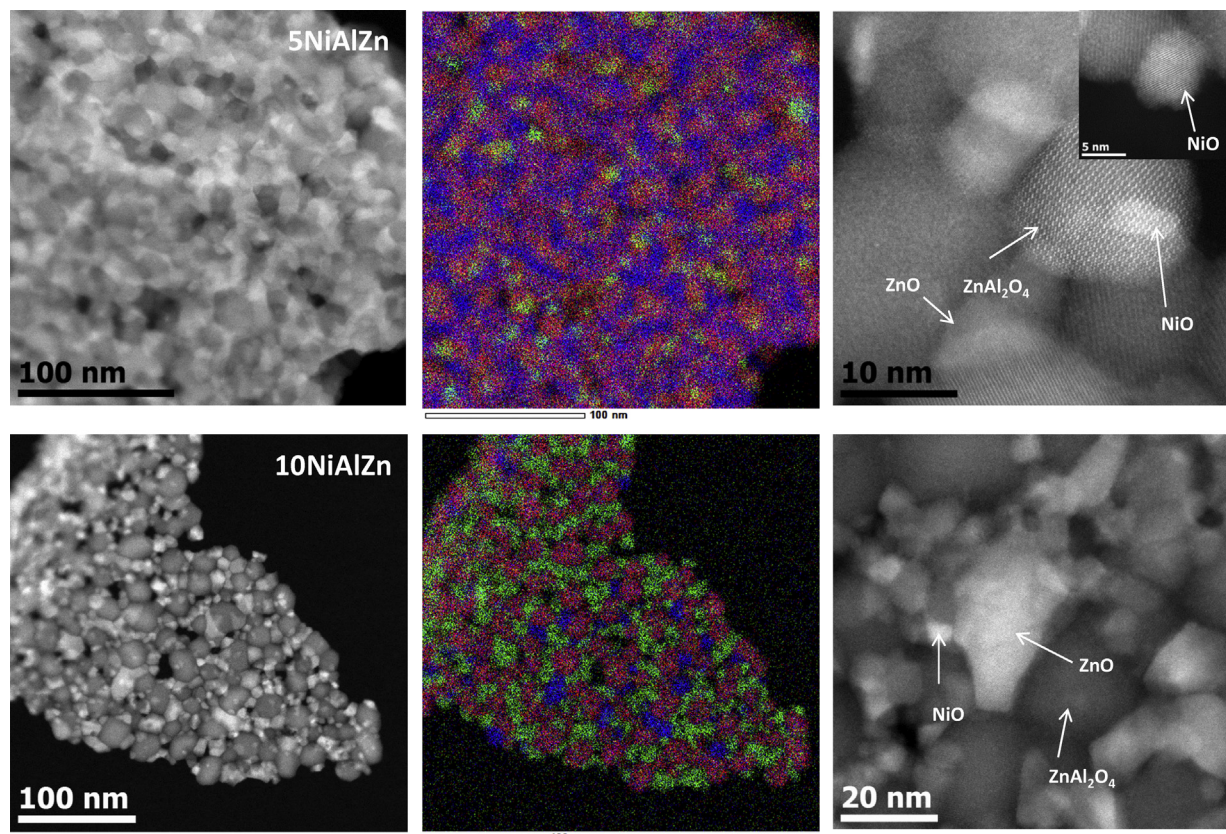
impregnation method [13]. These small crystallites lead to high dispersion of the nickel species on the support surface, enhancing the catalytic performance during the partial oxidation of ethanol.

Fig. 2 presents TEM micrographs of 5NiAlZn and 10NiAlZn calcined at 700 °C. The micrographs clearly show homogeneous and well defined spherical particles of 5–20 nm in size. The homogeneity of the system was confirmed by EDX measurements using a finely focused beam. Fig. 2 places the micrograph image from which the chemical maps were derived adjacent to two-dimensional chemical maps/spectral images for Al (red), Zn (blue), and Ni (green). According to the distribution of Zn and Al, the major part of the system consists indeed of pure ZnAl<sub>2</sub>O<sub>4</sub> spinel and ZnO phases, respectively. Some areas present a small excess of NiO identified by bright zones in the micrographs. Comparing the TEM micrographs of 5NiAlZn and 10NiAlZn, one can see that the material's morphology is similar to a spherical particle shape. However, a clear increase of NiO particle size with increased nickel loading is detected.

The surface chemistry of the materials has been studied by XPS analysis to investigate the elemental composition of the surface and the chemical state of these elements. The surface of all fresh catalysts was analyzed, and the surface of the catalysts used in standard tests was analyzed exclusively for 5NiAlZn and 20NiAlZn, because the catalytic behavior of 10NiAlZn is similar to that of 5NiAlZn. The relevant core–shell binding energies ( $E_B$ ) and Auger kinetic energies ( $E_K$ ) of the electrons are summarized in Table 2, and the corresponding spectra of the fresh catalyst samples are shown in Figs. 3 and 4. The spectra of the used catalyst samples are very similar to these. Comparison of the energies obtained shows that the values of the catalyst samples after test are shifted towards higher binding energy (lower kinetic energy) relative to those of the fresh samples. The magnitude of this shift is between 0.5 and 1.5 eV. Residual charging effects that were not eliminated by the charge correction are the most likely cause of the energy shift between the fresh and the used samples.

The Zn 2p<sub>3/2</sub> and the Zn LMM Auger spectra of the fresh catalyst samples are shown in Fig. 3. Because the Zn 2p<sub>3/2</sub> peak positions of Zn, ZnO, Zn(OH)<sub>2</sub>, and ZnAl<sub>2</sub>O<sub>4</sub> are very close in energy [22–24], the Zn L<sub>3</sub>M<sub>45</sub>M<sub>45</sub> Auger peak was also used to determine the type of zinc in the catalyst samples. In all cases this Auger peak had an asymmetric shape corresponding to that of oxidized Zn [23–26]. It was fitted with two peaks, with the main peak at ~988 eV and the shoulder peak at ~991 eV, in agreement with the literature [25]. The modified Auger parameters correspond most closely to that of ZnO [22–24], and the sample data points are located in the ZnO region on the Wagner plot (Fig. 3). The data for Zn, Zn(OH)<sub>2</sub>, ZnAl<sub>2</sub>O<sub>4</sub> and ZnO shown in the Wagner plot were obtained from the literature [22–25,27–29]. Thus, the zinc is in the form of ZnO in all samples, but the presence of ZnAl<sub>2</sub>O<sub>4</sub> cannot be ruled out. Of some note is the 20NiAlZn sample after test: it appears slightly separated from the ZnO region on the Wagner plot with lower Zn L<sub>3</sub>M<sub>45</sub>M<sub>45</sub> kinetic energy and higher Zn 2p<sub>3/2</sub> binding energy, but still with the same modified Auger parameter as ZnO. The intensity of all Zn peaks decreased significantly in the spectra of the samples after test compared to those of the fresh samples. This indicates that the Zn retreats from the surface into the bulk during the catalytic tests.

**Fig. 1.** XRD patterns of the calcined metal oxides.



**Fig. 2.** TEM micrograph of the xNiAlZn system calcined at 700 °C. (For interpretation of the references to color in the text, the reader is referred to the web version of this article.)

The Ni 2p spectra of the fresh catalysts are shown in Fig. 4. Comparison with the spectra of Ni, NiO, Ni(OH)<sub>2</sub>, and NiAl<sub>2</sub>O<sub>4</sub> given in [30] shows that Ni is present in an oxidized form in all samples. The main Ni 2p<sub>3/2</sub> peak does not show the double peak structure typical for NiO [30,31], and the binding energy difference between the main Ni 2p<sub>3/2</sub> peak and the satellite is  $6.1 \pm 0.1$  eV, corresponding to the value for NiAl<sub>2</sub>O<sub>4</sub> [32]. The Ni 2p<sub>3/2</sub> and Ni 3p main peak positions of the fresh catalyst samples are slightly below the range of values reported for NiAl<sub>2</sub>O<sub>4</sub> [31,32], while those of the catalysts after test fall within this range. These results indicate that the Ni in all catalyst samples is in the form of NiAl<sub>2</sub>O<sub>4</sub>, in contrast to the XRD data. However, the presence of NiO cannot be ruled out: the double peak structure of NiO might not be resolved due to peak broadening caused by sample charging.

The O 1s region is interesting in mixed oxides, since oxygen is present in several different chemical environments, which all contribute to the O 1s spectrum. The asymmetry of the O 1s peak (Fig. 4) clearly shows that several oxygen species are present in the catalyst samples; two peaks are required to fit the spectra. The peak at lower binding energy ( $530.1 \pm 0.4$  eV) can be assigned to NiO and ZnO [23–25,29–34], and the peak at higher binding energy ( $532.1 \pm 0.3$  eV) to Al<sub>2</sub>O<sub>3</sub>, NiAl<sub>2</sub>O<sub>4</sub>, ZnAl<sub>2</sub>O<sub>4</sub>, and the hydroxides Al(OH), Al(OH)<sub>3</sub>, Ni(OH)<sub>2</sub>, and Zn(OH)<sub>2</sub> [23,24,30–43]. However, the energy difference ( $\sim 2$  eV) between the peaks is larger than expected from the literature values ( $\sim 1.5$  eV). The relative amount of each oxygen species can be determined from the peak area using the relative sensitivity factor (O 1s: 0.78) for the Kratos Axis HS that is supplied by CasaXPS [17]. For the fresh catalyst samples, the

**Table 2**  
Core shell binding energies and Auger kinetic energies of the fresh catalysts (white background) and the catalysts used in standard tests (grey background).

Samples	Binding energy (eV), $E_B$				Kinetic energy (eV), $E_K$		Modified Auger parameter (eV), $\alpha' = E_B + E_K$	
	Al 2p	Zn 2p <sub>3/2</sub>	O 1s	Ni 2p <sub>3/2</sub> Ni 2p <sub>3/2</sub> (sat)	Zn L <sub>3</sub> M <sub>45</sub> M <sub>45</sub>	Al KLL	Zn 2p <sub>3/2</sub> –L <sub>3</sub> M <sub>45</sub> M <sub>45</sub>	Al 2p-KLL
5NiAlZn fresh	73.2	1021.6	530.2 532.2	855.0 861.1	988.5	1389.0	2010.1	1462.2
5NiAlZn after stability	74.6	1022.3	529.6 531.5	856.4 862.5	987.4	1387.1	2009.7	1461.7
5NiAlZn after test	74.4	1022.3	529.5 531.6	856.0 862.1	987.4	1387.4	2009.7	1461.8
10NiAlZn fresh	73.4	1021.7	530.1 532.0	855.1 861.2	988.5	1388.5	2010.2	1461.9
20NiAlZn fresh	73.4	1021.7	530.1 532.0	855.0 861.1	988.5	1388.8	2010.2	1462.2
20NiAlZn after test	74.9	1022.8	530.6 532.5	856.5 862.7	987.3	1386.7	2010.1	1461.6

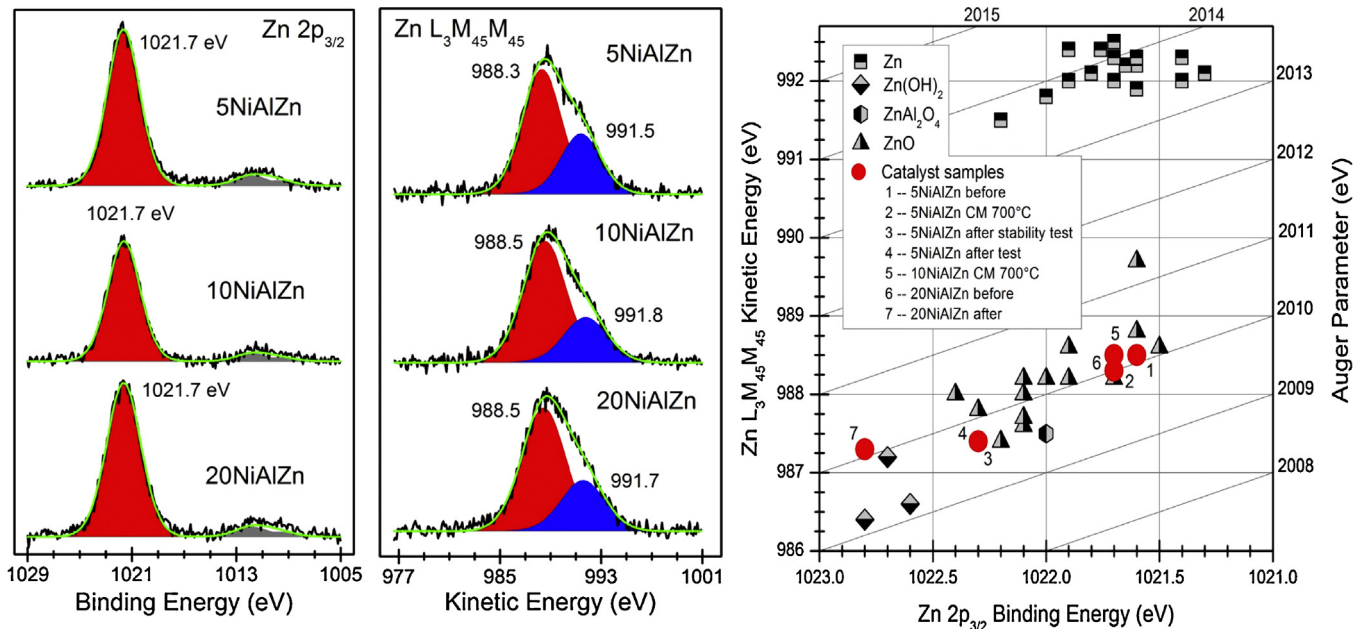


Fig. 3. The Zn 2p<sub>3/2</sub> (left) and Zn L<sub>3</sub>M<sub>45</sub>M<sub>45</sub> Auger (center) spectra of the fresh catalyst samples, and the Wagner plot (right) constructed from the main peaks.

amount of oxygen with the higher O 1s binding energy increases with increasing amount of Ni in the sample, from 16% for fresh 5NiAlZn to 28.5% for fresh 20NiAlZn. In the catalysts after test, most oxygen atoms (>80%) have the higher O 1s binding energy, indicating a structural change in the samples during the catalytic tests. The peak at 532 eV is mainly due to the presence of hydroxide. The intensity of peak increases after reaction, and this is a clear consequence of the high reaction temperature in presence of water produced by the RWGS. This correlates with the intensity reduction of the Zn peaks, supporting that Zn in the form of ZnO retreats from the surface into the bulk during the catalytic tests. However, some of the intensity of the 532.1 eV peak of the used samples is also due to SiO<sub>2</sub> (O 1s:  $E_B = 532.5$ –532.9 eV [40]), since the sam-

ples were diluted with quartz chips for the catalytic tests to avoid adverse thermal effects.

The Ni 3p, Al 2p, and Zn 3p peaks are fairly close in binding energy (Fig. 4), and the Al KLL Auger peak caused by bremsstrahlung excitation appears in this region as well. In fact, the Ni 3p and Al 2p peaks are so close in binding energy that they partially overlap. However, the nickel concentration in the catalyst samples is sufficiently low that the Al 2p peak is well resolved. The Al 2p binding energy of the used samples (Table 2) falls in the region for oxidized Al, notably Al<sub>2</sub>O<sub>3</sub> (73.5–75.6 eV) [24,31,33,36–44], AlO(OH) (74.0–74.2 eV) [39–41,44], Al(OH)<sub>3</sub> (73.8–74.6 eV) [39–46], NiAl<sub>2</sub>O<sub>4</sub> (73.8–74.8 eV) [31–35], and ZnAl<sub>2</sub>O<sub>4</sub> (74.5 eV) [24]. In contrast, the fresh samples have an Al

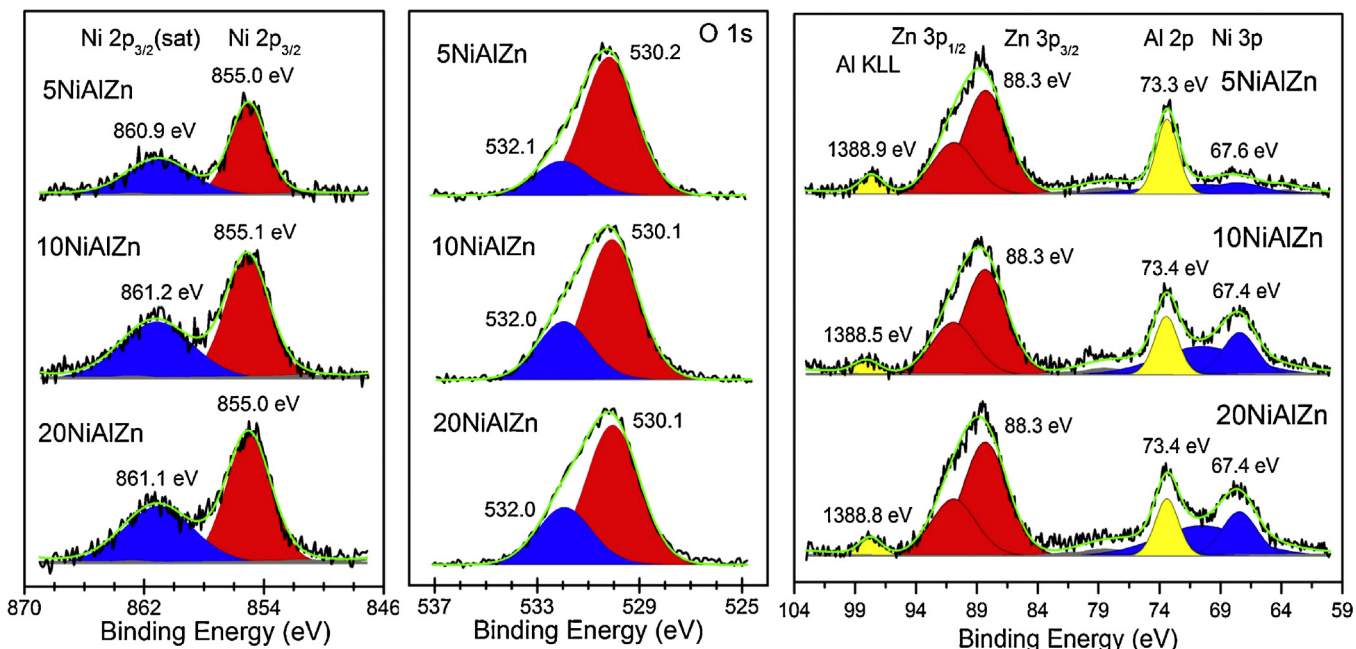


Fig. 4. The Ni 2p<sub>3/2</sub> (left), the O 1s (center), and the Zn 3p, Al 2p, and Ni 3p (right) spectra of the fresh catalyst samples.

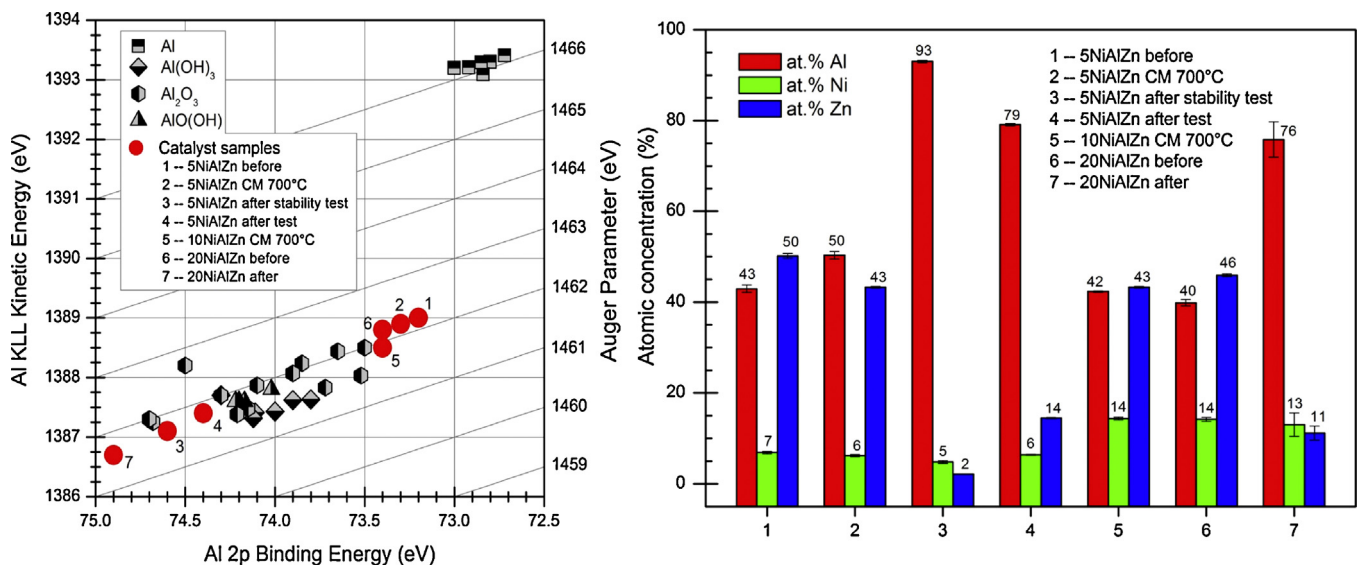


Fig. 5. The Wagner plot constructed from the Al 2p photoelectron and the Al KLL Auger peaks (left) and the relative abundance of the metals at the surface of the catalyst samples determined from the areas of the Ni 3p, Al 2p and Zn 3p peaks (right).

2p binding energy slightly lower than oxidized Al (73.5–75.6 eV), but higher than metallic Al (72.5–73.0 eV) [44–26]. The Wagner plot constructed from the Al 2p and the Al KLL lines (Fig. 5), however, reveals that the Al in the fresh samples is also in the oxidized form. Combining this with the information from the Ni 2p spectra indicates that the Al in the catalyst samples is most likely in the form of  $\text{NiAl}_2\text{O}_4$ . However, other species, in particular  $\text{Al}_2\text{O}_3$  and  $\text{ZnAl}_2\text{O}_4$ , cannot be ruled out.

Peak areas can be used to determine the concentration of each element at the sample surface, especially if the peaks have comparable kinetic energies, and thus similar surface sensitivity, as is the case for the Al 2p, Ni 3p and Zn 3p lines. The relative concentrations of Al, Ni, and Zn was calculated from the peak areas of these three lines (Al 2p peak, Ni 3p main peak at ~68 eV, and the total area of both Zn 2p peaks) using the relative sensitivity factors (Al 2p: 0.193, Ni 3p: 0.598, Zn 3p: 0.939) for the Kratos Axis HS that are supplied by CasaXPS [17], and the results are shown in Fig. 5. The different elemental composition of the metals at the surface of the fresh and the used catalyst samples suggests that the surface composition has changed: Al becomes more abundant at the surface, while Zn retreats into the bulk during the catalytic test. This variation of surface concentration of key elements before and after the catalytic test confirms the indicated structural modification of the samples.

The C 1s spectra are composed of a single peak. It was used as charge reference – its position was set to 284.8 eV – and it is assigned to adsorbed carbonaceous matter (adventitious C). The fresh samples have an additional very low intensity peak at  $289.2 \pm 0.2$  eV that can be assigned to adsorbed carbonates [47–49], probably a residue from the preparation process. Based on the peak areas (relative sensitivity factors: C 1s = 0.278, O 1s = 0.78, Al 2p = 0.193, Ni 3p = 0.598, Zn 3p = 0.939 [17]), ~30% of the near-surface atoms are carbon, and most (~95%) of this carbon is in the form of adventitious C. Apart from the disappearance of the carbonate peak after the catalytic tests, no changes were observed in the C 1s spectra.

In order to quantify carbon deposition, the used catalysts were subjected to CHNS analysis. The carbon content of all catalysts was less than 0.05 wt% indicating that carbon formation did not have a detrimental influence in the partial oxidation of ethanol at the temperature range of 600–750 °C. After the long-term stability test over

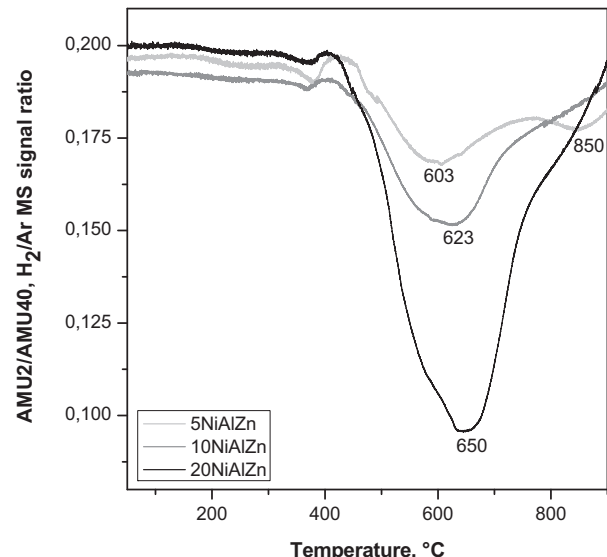


Fig. 6. The MS hydrogen signal as a function of temperature recorded in the TPR analysis performed on calcined metal oxides.

the 5NiAlZn catalyst the carbon amount was only 0.3 wt% demonstrating the high resistance of xNiAlZn catalysts to coking.

### 3.2. Redox behavior of the catalyst

Reducibility of NiO species and their interaction with the support were studied in TPR experiments. It is evident from the TPR curves (Fig. 6) that the catalysts consume hydrogen in three temperature ranges. The first and minor peak in the 370–390 °C interval is assigned to the reduction of loosely attached NiO crystals, but their fraction in the total amount of NiO species is low based on the relative peak areas. The second and the major event characterized by a broad peak with a maximum in the 600–650 °C range arises from the reduction of NiO species possessing stronger interaction with the support. The fact that the peak is broad and asymmetric indicates the presence of a multitude of such NiO species with different strength of binding to the support. It is emphasized in the

literature that the reducibility of NiO species in catalysts strongly depends on the strength of their interaction with a support [50]. The shift of the maximum from 603 to 650 °C with increasing Ni loading appears counterintuitive because the larger NiO particles formed on the surface of the materials with higher Ni content should have weaker interaction with the support. However, reduction kinetics may also play a role: the core of large NiO particles will be reduced at higher temperatures than the outer layers merely because of a longer diffusion pathway of oxygen.

The third event appears at high temperature and it is only resolved clearly in the case of 5NiAlZn where a maximum at 850 °C is obtained. On the 10NiAlZn and 20NiAlZn samples it manifested itself as a shoulder of the major event on the high-temperature side. This event should be assigned to the reduction of the NiAl<sub>2</sub>O<sub>4</sub> phase [51], whose presence was established in our samples by XRD and TEM analysis. The shift of the reduction event to the lower temperatures at higher Ni loading may be explained by increasing hydrogen spillover that enhanced the reduction of Ni in the support lattice. Indeed, higher Ni loading results in a higher surface coverage with NiO species which are mostly converted to metallic Ni at 650 °C. The latter is known to facilitate hydrogen spillover and cause support reduction as demonstrated in our previous work [13].

For comparison, pure AlZn mixed oxide was also analyzed by TPR. No hydrogen consumption took place in the tested temperature range (up to 900 °C). Hence, the events observed on the Ni-containing materials were actually the reduction of the NiO species.

Summarizing the findings made in the physico-chemical characterization experiments, the following should be emphasized:

- i. TEM analysis revealed that all catalysts have similar morphology, i.e., spherical polycrystalline particles which, however, differed in size from 5 to 20 nm. ED and XRD analyses of xNiAlZn revealed the presence of NiO, ZnAl<sub>2</sub>O<sub>4</sub> spinel, and ZnO in the respective materials.
- ii. The TPR analysis indicates that nickel oxide in xNiAlZn is most likely present as highly dispersed NiO particles. The interaction between nickel species and support increases with increasing nickel loading.
- iii. By XPS analysis it was demonstrated that the Ni at the sample surface appears in the form of NiAl<sub>2</sub>O<sub>4</sub> and possibly NiO. XPS analysis of the fresh and the used samples shows clearly that the atomic concentration of Zn, Ni and Al at the surface is changed during the reaction. Alumina becomes more abundant at the surface, while Zn retreats into the bulk after the catalytic test. The amount of nickel at the surface remains constant.

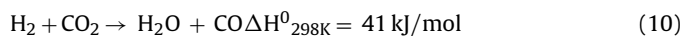
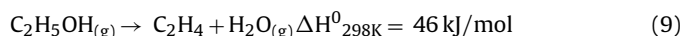
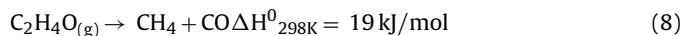
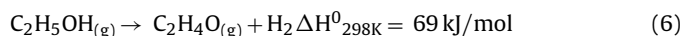
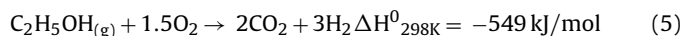
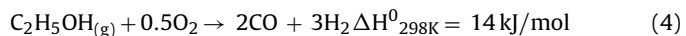
### 3.3. Catalytic performance

The catalytic properties of the blank AlZn and the xNiAlZn catalysts at temperatures of 600–750 °C, atmospheric pressure, and an oxygen-to-ethanol molar ratio of 0.75 are summarized in Table 3. The activity of the catalysts with different Ni loading and the product distribution were compared after maintaining the reaction for 2 h at each temperature. The experimental tests were carried out without previous reduction of the catalysts.

Ethanol conversion over the blank AlZn increased with temperature achieving 98% at 750 °C. Analysis of the product composition revealed that the dehydrogenation of ethanol to acetaldehyde is the main reaction at low temperature (400–500 °C), and dehydration yielding ethylene occurs at a lower rate [13]. At 600 °C product distributions changed dramatically: the selectivity to acetaldehyde decreased strongly to near zero along with increasing selectivities to CO, H<sub>2</sub>, CO<sub>2</sub> and CH<sub>4</sub>. Above 600 °C, the product mixture did not contain any acetaldehyde, but a mixture of CO and CO<sub>2</sub> was formed along with H<sub>2</sub>, according to the overall Eqs. (4) and (5). At higher

temperatures the dehydration of ethanol was promoted, too. As a result, a significant amount of ethylene is produced on the blank catalyst.

Obviously, the amphoteric character of the support determines the pathway of the partial oxidation reaction and the product distribution. The presented systems (AlZn and xNiAlZn) exhibit a stable ZnAl<sub>2</sub>O<sub>4</sub> spinel phase and metal oxides which are formed during calcination. Mixed oxide phases between support and active metal were also formed. Using this type of catalyst, bio-ethanol is converted on the spinel phase at temperatures above 400 °C via dehydrogenation to acetaldehyde and hydrogen (Eq. (6)), followed by acetaldehyde partial oxidation (Eq. (7)) or decomposition (Eq. (8)). Thus ethylene formation by dehydration according to Eq. (9) at low temperature can be prevented and therefore, coke formation is reduced. These reactions occur in parallel with the partial oxidation and influence the hydrogen yield. However, the partial oxidation of ethanol to CO and H<sub>2</sub> (Eq. (4)) becomes more significant at higher temperatures when it is thermodynamically favored. CO is also produced from reverse water gas shift reaction (Eq. (10)) at high temperatures, which leads to the formation of water by consuming hydrogen and CO<sub>2</sub>. A syngas-like gas is produced at high temperatures which can be used for power generation in fuel cell applications.



The presence of nickel increases the effectivity of the catalyst in the partial oxidation of ethanol due to its high activity for the cracking of CC bonds. The Ni catalysts showed very high activity with high ethanol conversion at 600 °C and complete conversion for temperatures above 700 °C, respectively. Nevertheless, the increased nickel loading affected the ethanol conversion only negligibly, because it was quite high in the temperature range of 600–750 °C. Furthermore, excellent selectivities towards H<sub>2</sub> and CO as the desired products were obtained. A selectivity of about 80% toward hydrogen was observed at 600 °C, and ~90% was obtained at 750 °C. However, maximum H<sub>2</sub> selectivity was achieved at 700 °C, while the further increase of reaction temperature results in a loss of hydrogen. This indicates that at high temperature the water gas shift reaction dominates, leading to a lower H<sub>2</sub> and CO<sub>2</sub> selectivity and accordingly higher CO selectivity. As the main byproducts, CO<sub>2</sub> and methane were observed with decreasing selectivity at increasing temperature. Other byproducts, such as acetaldehyde and ethylene were detected in lower amounts, and their selectivity at 750 °C was negligible. Generally, it is concluded that with rising temperature the formation of CH products is decreased, thus increasing the hydrogen selectivity. Coke formation was not relevant during the reaction at high temperature. The very high selectivity towards CO compared to the selectivity towards CO<sub>2</sub> indicates reasonably good ability of the catalyst to promote the reversed water gas shift reaction.

The results reveal that Ni loading has an important effect on the product distribution. The highest selectivities to H<sub>2</sub> and CO were obtained using the 5NiAlZn catalyst, but also the 10NiAlZn catalyst showed high catalytic performance. At full ethanol conversion, the selectivity towards H<sub>2</sub> slightly decreased with increasing Ni loading. The same effect was observed for the selectivity to

**Table 3**

Catalyst performance in the partial oxidation of ethanol at different temperature.

Samples	Temperature		Conversion (%)	Selectivity						C balance (%)
	oven (°C)	reactor (°C)		H <sub>2</sub> (%)	CO (%)	CO <sub>2</sub> (%)	CH <sub>4</sub> (%)	C <sub>2</sub> H <sub>4</sub> (%)	CH <sub>3</sub> CHO (%)	
AlZn	600	770	90	30	35	28	9	25	0	97
	700	850	95	25	38	28	8	26	0	100
	750	880	98	25	39	28	7	26	0	100
5NiAlZn	600	770	98	88	79	16	3	3	0	98
	700	850	100	90	92	10	2	0	0	100
	750	880	100	90	94	8	1	0	0	100
10NiAlZn	600	770	98	77	77	10	3	7	4	100
	700	850	99	80	85	10	3	2	1	100
	750	880	100	80	91	8	2	0	0	99
20NiAlZn	600	770	99	80	69	15	5	8	4	100
	700	850	100	78	78	12	4	4	2	100
	750	880	100	75	85	11	4	2	1	100

CO. Otherwise, the formation of CH containing byproducts such as methane, ethylene or acetaldehyde increased with increasing Ni loading. Over the 5NiAlZn and 10NiAlZn catalysts, neither acetaldehyde nor ethylene were detected at the highest temperature tested (750 °C). In contrast, further increase of Ni loading to 20 wt% remarkably improves side reactions. As a consequence, greater amounts of CH containing by-products were formed, and the selectivities toward H<sub>2</sub> and CO were lower.

The Ni content influences the dispersion behavior of nickel particles on the support, and thus, the product distribution in the partial oxidation of ethanol is affected. It is interesting to observe that a high Ni loading (20 wt%) not only promotes methane production but also increases the amount of other byproducts. Obviously, with higher Ni content the catalytic performance of the catalyst declined due to the larger NiO crystallite size (see Table 1) and the formation of the NiAl<sub>2</sub>O<sub>4</sub> phase at the surface, which is evident after XRD and TEM analysis. The interaction between nickel species and support increases with increasing nickel loading. XPS analysis revealed a change in the atomic concentration of Zn, Ni, and Al at the surface under reaction conditions, and this probably determines the catalytic behavior of the samples.

As shown above, the addition of nickel significantly influences the catalytic activity and selectivity. Obviously, the presence of only small amounts of nickel promotes substantially the production of syngas by partial oxidation of ethanol. Therefore, the 5NiAlZn and 10NiAlZn catalysts were subjected to long-term experiments to determine catalyst stability. In Fig. 7 the catalytic activity and the selectivity of the reaction of the respective catalyst materials at 700 °C are shown over a period of 100 h.

Both catalysts showed high stability under the given reaction conditions. However, the catalyst with the lower Ni loading is the more active and stable. Full ethanol conversion was achieved over the 5NiAlZn catalyst during 100 h on stream with the main products being H<sub>2</sub>, and CO with a selectivity of about 90% and 92%, respectively. The amount of CO<sub>2</sub> in the reaction mixture was usually less than 10%, and decreases with time-on-stream. CH containing products were observed in small amounts (S < 5%). Together with partial oxidation of ethanol, products of RWGS reaction are detected during stability test.

The tendency for syngas production was influenced by Ni loading. Using the 10NiAlZn catalyst, the ethanol conversion achieved 98% and was constant during the 100 h on-stream. The 10NiAlZn catalyst affected a slightly different product distribution compared to the 5NiAlZn catalyst. The selectivity to H<sub>2</sub> was in the range of 70–78% and decreased slightly with increasing time-on-stream. This effect is caused by the increasing formation of CH containing byproducts such as methane (~5%) and ethylene (~5%).

The selectivity to CO remained nearly constant at 85% during 100 h time-on-stream, while the selectivity to CO<sub>2</sub> showed a slight decline in the range of 10–8%. A reduced H<sub>2</sub> selectivity at higher nickel loading most likely results from the fact that high Ni loading leads to particle agglomeration. This finding is in agreement with results reported by Tsay and Chang [52] showing a higher dispersion in catalysts of low Ni loading compared to those with a high Ni loading, as well as an overall decrease in dispersion with increasing Ni content. Large Ni particles in catalysts of high Ni content may result in the blockage of carrier pores limiting the availability of active sites on the catalyst, thereby hindering selectivity and performance in the partial oxidation reaction of ethanol.

The very harsh SOFC operation conditions, i.e., the high temperature and the exposed chemical environments, require further stability tests. In addition to long-term stability tests, the stability of the Ni catalyst was studied by means of simulated start-stop operation cycles during the partial oxidation reaction to simulate thermal cycles during the fuel cell lifetime. The 5NiAlZn catalyst was exposed to at least 4 start-stop cycles performed at temperatures between room temperature and 600–750 °C. An initial cycle of catalyst operation was run stepwise at 600–750 °C for 6 h, followed by an operational stop mode with the catalyst being kept at room temperature for about 16 h. The simulated start-stop cycles were operated 4 times with an overall operation time of about 100 h. The catalyst performance over the thermal cycles is presented in Fig. 8. In the first cycle an ethanol conversion of about 99% was observed at 600 °C, and 100% conversion was obtained at 700 °C. With increasing number of thermal cycles a slight decline in ethanol conversion at 600 °C was observed. However, complete ethanol conversion was achieved in all processing steps at the final reaction temperature of 750 °C. Fig. 8 also shows the influence of reaction conditions on the selectivities toward hydrogen as well as the other products detected. It is evident that the increase of temperature in every cycle led to increasing selectivities towards H<sub>2</sub> and CO, while the CO<sub>2</sub> selectivity decreased. Most importantly, the product distribution is affected by the number of start-stop operations. With increasing number of thermal cycles, the selectivity to hydrogen and CO decreased while the selectivity to CO<sub>2</sub> increased. The stronger decrease of the H<sub>2</sub> selectivity compared to that of CO indicates the consumption of hydrogen, possible by the reverse water gas shift reaction. This is confirmed by the decline in the selectivity to CO<sub>2</sub>. Otherwise, the selectivity to CO was not increased. Hence, hydrogen producing reactions such as ethanol partial oxidation (Eqs. (4) and (5)), but also ethanol dehydrogenation (Eq. (6)) are suppressed with increasing number of thermal cycles, and undesired reactions are more favored. This leads to the formation of more CH containing products, such as ethylene which is formed by

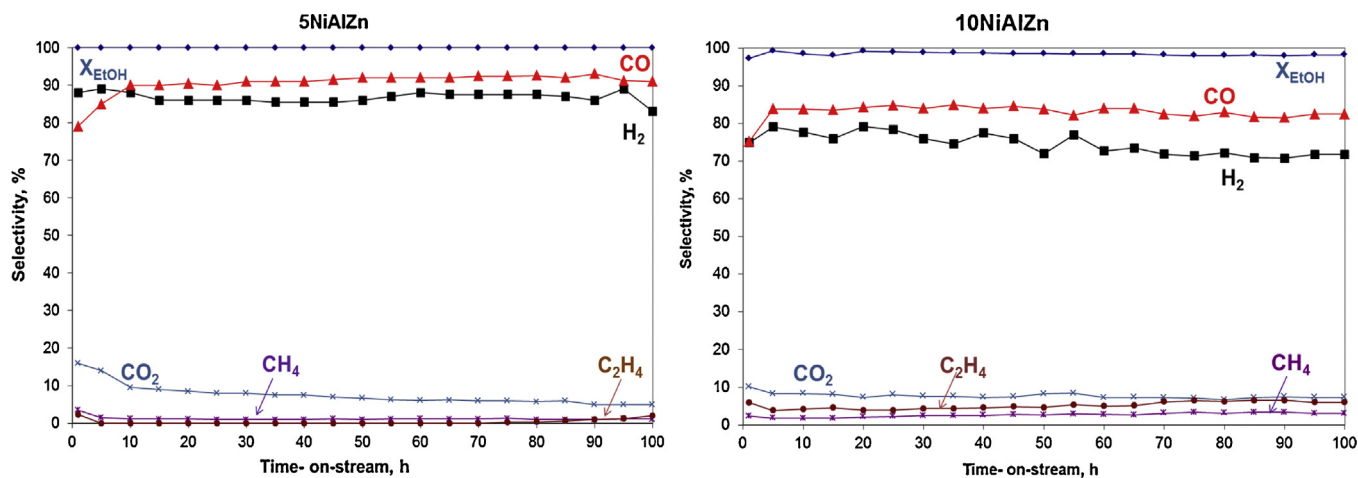


Fig. 7. Long-term stability test of the 5NiAlZn and 10NiAlZn catalysts in the partial oxidation of ethanol ( $T = 700^\circ\text{C}$ ,  $\text{O}_2/\text{ethanol}$  molar ratio = 0.75, GHSV = 35,000  $\text{h}^{-1}$ ,  $p = 1$  bar).

ethanol dehydration or methane formed by decomposition reactions. Obviously, the ethylene selectivity increased strongly with increasing number of cycles. To summarize, the catalyst exhibits high activity and long-term stability without noteworthy degradation, but a slight deactivation in start-stop cycles simulating the thermal conditions of the SOFC under harsh conditions was observed.

Finally, the 5NiAlZn catalyst was used to investigate the effect of the oxygen-to-fuel molar ratio on the POE ranging from 0.6 to 0.9 at a constant temperature of  $700^\circ\text{C}$ . Independent of the applied molar ratio, complete ethanol conversion was obtained. However, the selectivity of the reaction was affected. The corresponding results are shown in Fig. 9. The main products  $\text{H}_2$  and  $\text{CO}$  were detected, as well as  $\text{CO}_2$  as byproduct (Fig. 9, left). Other byproducts, such as methane, acetaldehyde, and ethylene were formed only in small amounts (Fig. 9, right). For all experiments hydrogen selectivities above 80% were observed with a maximum of 89% at a  $\text{O}_2/\text{ethanol}$  molar ratio of 0.75 (Fig. 9, left). The selectivity to  $\text{CO}$  shows a similar tendency, also revealing a maximum

(92%) at the molar ratio of 0.75. With rising oxygen supply, oxidation reactions are favored leading to a continuous increase of the  $\text{CO}_2$  selectivity. Consequently, the selectivity to CH containing byproducts decreased. At a molar ratio of 0.9 both ethylene and acetaldehyde were not detected, and the selectivity to methane was <2%. Otherwise, with decreasing oxygen supply the formation of hydrocarbons such as methane or ethylene, and other CH containing products such as acetaldehyde was enhanced, while the selectivity to the oxidized products decreased strongly. The formation of  $\text{CO}_2$  was not observed at molar ratios less than 0.7. That means that the oxygen supply was not sufficient for the ethanol partial oxidation according to Eq. (5).

Based on these results, an oxygen-to-fuel molar ratio of 0.75 was identified as most suitable for the POE over the 5NiAlZn catalyst, providing a syngas with maximum selectivity to  $\text{H}_2$  and  $\text{CO}$  at comparably low selectivity to  $\text{CO}_2$ , which can be used to feed the anode of a SOFC. Furthermore, the addition of a slight excess of oxygen is known to suppress coke formation, which is mainly formed by the polymerization of ethylene and oxygenates. The CHNS elemental

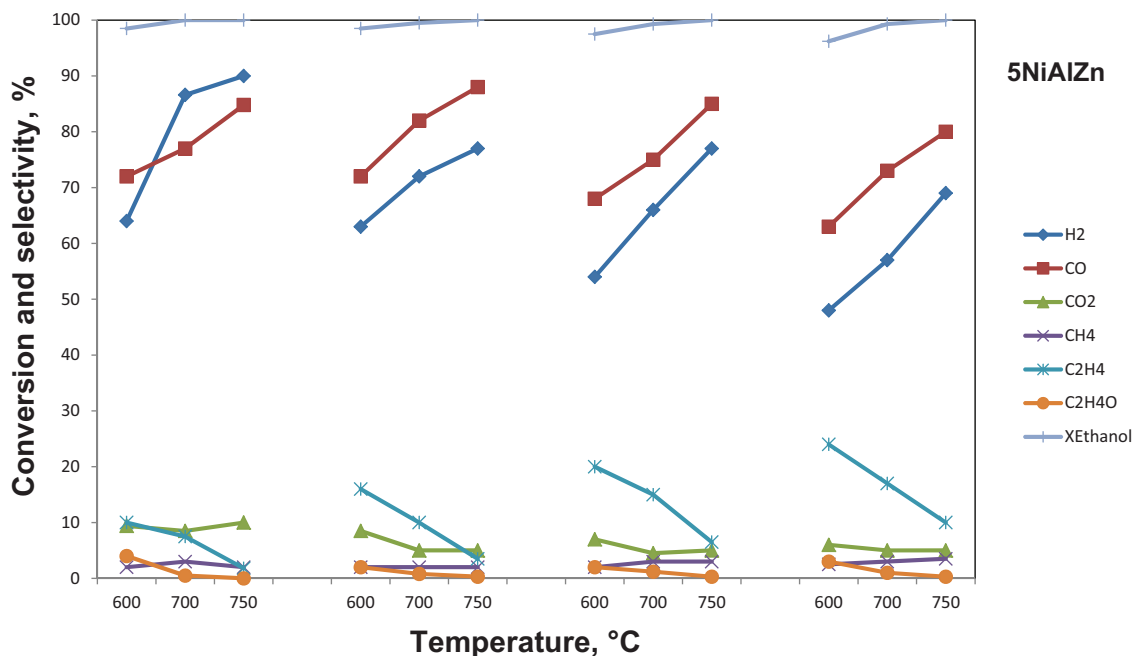
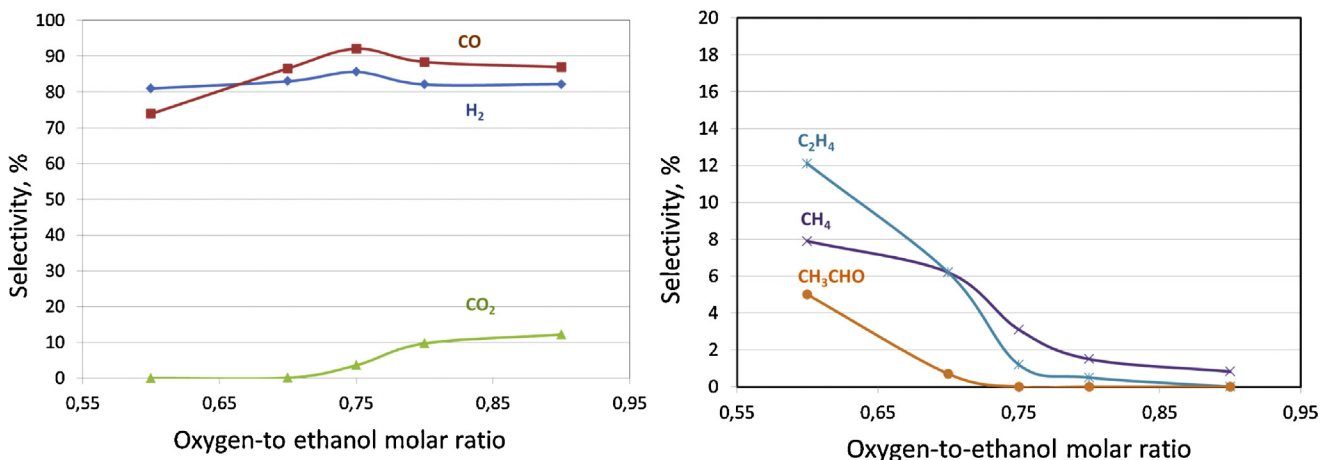


Fig. 8. Thermal cycle stability of the 5NiAlZn catalyst in the partial oxidation of ethanol ( $T = 700^\circ\text{C}$ ,  $\text{O}_2/\text{ethanol}$  molar ratio = 0.75, GHSV = 35,000  $\text{h}^{-1}$ ,  $p = 1$  bar).



**Fig. 9.** Product distribution in the partial oxidation of ethanol over the 5NiAlZn catalyst as a function of the molar ratio O<sub>2</sub>/ethanol ( $T = 700^\circ\text{C}$ , GHSV = 35,000 h<sup>-1</sup>,  $p = 1$  bar); selectivity to H<sub>2</sub>, CO, and CO<sub>2</sub> (left) and to C<sub>2</sub>H<sub>4</sub>, CH<sub>4</sub>, and CH<sub>3</sub>CHO (right).

analysis of the used 5NiAlZn sample revealed a carbon content of only 0.05 wt%.

#### 4. Conclusions

In this study, hydrogen generation by partial oxidation of bioethanol over catalysts with different Ni loading was investigated under variation of the reaction parameters. Based on the above results the following conclusions can be drawn:

- 1 The xNiAlZn catalysts, synthesized by a modified sol–gel method using citric acid as complexing agent, showed high catalytic activity and selectivity in the partial oxidation of ethanol. A hydrogen and CO rich gas is obtained which can be used to feed the anode of a fuel cell of SOFC type.
- 2 A NiAlZn catalyst with only 5 wt% Ni can effectively catalyze the partial oxidation of ethanol. Ethanol is completely converted at 700 °C with high selectivity to H<sub>2</sub> and CO. Besides the produced syngas, only CO<sub>2</sub> is formed as a byproduct, while the amount of methane and ethylene is negligible. Increasing the Ni loading leads to a lower selectivity with an increased formation of CH containing byproducts.
- 3 The best performance of the 5NiAlZn catalyst is attributed to the small crystallite size present in catalysts of low Ni loading, which facilitates a high, uniform dispersion of the metal particles on the support surface.
- 4 With increased Ni loading the ratio of ZnO and ZnAl<sub>2</sub>O<sub>4</sub> spinel structure shifts toward ZnO. Nickel is present in the catalyst as highly dispersed NiO particles. Their particle size increases with increasing metal loading. The XPS experiments show that after the catalytic reaction the alumina is more abundant at the surface, while Zn was drawn back into the bulk.
- 5 A molar ratio of O<sub>2</sub>/ethanol of 0.75 was shown to be the most promising ratio to obtain a syngas with maximal selectivity to hydrogen and CO. While with increasing oxygen supply oxidation reactions are favored which leads to a higher CO<sub>2</sub> selectivity, the formation of hydrocarbons such as methane or ethylene increased with decreasing oxygen supply.
- 6 The long-term stability of the catalyst was proved over 100 h time-on-stream at 700 °C without remarkable degradation. A slightly decreased H<sub>2</sub> selectivity is explained by an increasing formation of CH containing byproducts. However, the thermal stability in simulated start–stop cycles was not fully convincing. With increasing number of thermal cycles a slight decline in

ethanol conversion was observed, and the selectivity to hydrogen and CO decreased.

#### Acknowledgments

Financial support of this work was provided by the Federal state of Mecklenburg-Vorpommern (Project No. V-630-S-086-2010/255 and V-630-F-086/2010/256) and the Leibniz Organization. The authors thank Dr. Matthias Schneider and Dr. Sergey Sokolov from LIKAT for XRD and TPR measurements and discussion, and Dr. Roland Hergenröder from ISAS for assistance with the XPS measurements.

#### References

- [1] B. Huang, Y. Qi, M. Murshed, J. Process Control 21 (2011) 1426–1437.
- [2] Intergovernmental Panel on Climate Change, Climate Change: The Physical Science Basis, Cambridge University Press, 2007, 2007.
- [3] J.A. Turner, Science 305 (2004) 972–977.
- [4] M.C. Williams, Fuel Cells 7 (2007) 78–85.
- [5] H. Ehrich, E. Kraleva, M. Boltze, Proceedings of 11th European SOFC & SOE Forum 2014, B1510, chapter 18, p. 66–72, 1–4 July 2014, Lucerne, Switzerland, 2015.
- [6] G. Rabenstein, V. Hacker, J. Power Sources 185 (2008) 1293–1304.
- [7] W. Wang, Y. Wang, Int. J. Hydrogen Energy 33 (2008) 5035–5044.
- [8] L.V. Mattos, G. Jacobs, B.H. Davis, F.B. Noronha, Chem. Rev. 112 (2012) 4094–4123.
- [9] J.R. Salge, G.A. Deluga, L.D. Schmidt, J. Catal. 235 (2005) 69–78.
- [10] R. Gui-López, R.M. Navarro, M.A. Peña, J.L.G. Fierro, Int. J. Hydrogen Energy 36 (2011) 1512–1523.
- [11] S.M. de Lima, A.M. da Silva, L. da Costa, U.M. Graham, G. Jacobs, B.H. Davis, L.V. Mattos, F.B. Noronha, J. Catal. 268 (2009) 268–281.
- [12] A. Denis, W. Grzegorczyk, W. Gac, A. Machocki, Catal. Today 137 (2008) 453–459.
- [13] E. Kraleva, S. Sokolov, M. Schneider, H. Ehrich, Int. J. Hydrogen Energy 38 (2013) 4380–4388.
- [14] E. Kraleva, H. Ehrich, J. Sol–Gel Sci. Technol. 64 (2012) 619–626.
- [15] H. Ehrich, E. Kraleva, Cent. Eur. J. Chem. 12 (2014) 1285–1293.
- [16] E. Kraleva, S. Sokolov, G. Nasillo, U. Bentrup, H. Ehrich, Int. J. Hydrogen Energy 39 (2014) 209–220.
- [17] N. Fairley, CasaXPS: Processing software for XPS, AES, SIMS and More, version 2.3.15, Casa software Ltd., 2009. (Vision Axis (HS/Ultra/Nova) Element Library <http://www.casaxps.com/kratos/CasaXPS.lib.zip>).
- [18] M.F. Barroso, L.A. Arrúa, M.C. Abello, Appl. Catal. A: Gen. 304 (2006) 116–123.
- [19] T. Wigmans, J.A. Moulain, J. Chem. Soc. Chem. Commun. 4 (1980) 170–171.
- [20] A.J. Vizcaino, M. Lindo, A. Carrero, J.A. Calles, Int. J. Hydrogen Energy 37 (2012) 1985–1992.
- [21] S. Chenna, R. Banerjee, P.A. Crozier, Chemcatchem 3 (2011) 1051–1059.
- [22] L.S. Dake, D.R. Baer, J.M. Zachara, Surf. Interface Anal. 14 (1989) 71–75.
- [23] G. Deroubaix, P. Marcus, Surf. Interface Anal. 18 (1992) 39–46.
- [24] B.R. Strohmeier, D.M. Hercules, J. Catal. 86 (1984) 266–279.
- [25] B. Mutel, A. Ben Taleb, O. Dessaux, P. Goudmand, L. Gengembre, J. Grimalt, Thin Solid Films 266 (1995) 119–128.
- [26] A.B. Velichenko, J. Portillo, M. Sarret, C. Muller, Appl. Surf. Sci. 148 (1999) 17–23.

[27] M. Bär, A. Ennaoui, J. Klaer, T. Kropp, R. Saíez-Araoz, N. Allsop, I. Lauermann, H.W. Schock, M.C. Lux-Steiner, *J. Appl. Phys.* 99 (2006) 123501–123509.

[28] C.J. Powell, *J. Electron Spectrosc.* 185 (2012) 1–3.

[29] S. Bera, S. Dhara, S. Velmurugan, A.K. Tyagi, *Int. J. Spectrosc.* 2012 (2012) 1–4.

[30] R.B. Shalvoy, B.H. Davis, P.J. Reucroft, *Surf. Interface Anal.* 2 (1980) 11–16.

[31] P.H. Bolt, E. ten Grotenhuis, J.W. Geus, F.H.P.M. Habraken, *Surf. Sci.* 329 (1995) 227–240.

[32] K.T. Ng, D.M. Hercules, *J. Phys. Chem.* 80 (1976) 2094–2102.

[33] P. Lorenz, J. Finster, G. Wendt, J.V. Salyn, E.K. Žumadilov, V.I. Nefedov, *J. Electron Spectrosc.* 16 (1979) 267–276.

[34] L. Salvati Jr., L.E. Makovsky, J.M. Stencel, F.R. Brown, D.M. Hercules, *J. Phys. Chem.* 85 (1981) 3700–3707.

[35] S. Kasztelan, J. Grimbölt, J.P. Bonnelle, E. Payen, H. Toulhoat, Y. Jacquin, *Appl. Catal.* 7 (1983) 91–112.

[36] E. Paparazzo, *J. Electron Spectrosc.* 43 (1987) 97–112.

[37] B. Ealet, M.H. Elyakhloufi, E. Gillet, M. Ricci, *Thin Solid Films* 250 (1994) 92–100.

[38] C.D. Wagner, J.A. Taylor, *J. Electron Spectrosc.* 20 (1980) 83–93.

[39] J.A. Taylor, *J. Vac. Sci. Technol.* 20 (1982) 751–755.

[40] C.D. Wagner, *J. Vac. Sci. Technol.* 21 (1982) 933–944.

[41] O. Böse, E. Kemnitz, A. Lippitz, W.E.S. Unger, *Fresenius J. Anal. Chem.* 358 (1997) 175–179.

[42] S. Thomas, P.M.A. Sherwood, *Anal. Chem.* 64 (1992) 2488–2495.

[43] F. Rueda, J. Mendialdua, A. Rodriguez, R. Casanova, Y. Barbaux, L. Gengembre, L. Jalowiecki, *J. Electron Spectrosc.* 82 (1996) 135–143.

[44] C.D. Wagner, H.A. Six, W.T. Jansen, J.A. Taylor, *Appl. Surf. Sci.* 9 (1981) 203–213.

[45] J.A. Taylor, *J. Phys. Chem.* 75 (1981) 1735–1745.

[46] P.M.T.M. van Attekum, J.M. Trooster, *Phys. Rev. B* 18 (1978) 3872–3883.

[47] L. Sabatini, B. Morelli, P. Zambonini, B.A. DeAngelis, *J. Chem. Soc. Faraday Trans. 1* (75) (1979) 2628–2637.

[48] F. Garbassi, A.M. Marabini, *J. Chem. Soc. Faraday Trans. 1* (82) (1986) 2043–2055.

[49] Y. Jia, T. Luo, X.-Y. Yu, J.-H. Liu, X.-J. Huang, *New J. Chem.* 37 (2013) 534–539.

[50] S. Damyanova, B. Pawelec, K. Arishtirova, J.L.G. Fierro, *Int. J. Hydrogen Energy* 37 (2012) 15966–15975.

[51] M. Zaungouei, A.Z. Moghaddam, M. Arasteh, *Chem. Eng. Res. Bull.* 14 (2010) 97–102.

[52] M.T. Tsay, F.W. Chang, *Appl. Catal. A: Gen.* 203 (2000) 15–22.